RSC Advances

ROYAL SOCIETY OF CHEMISTRY

www.rsc.org/advances

Sonochemical synthesis of reduced graphene oxide uniformly decorated with hierarchical ZnS nanospheres and its enhanced photocatalytic activities

A. Moradi Golsheikh[1, 2*], H.N. Lim[3], Rozalina Zakaria[4], N.M. Huang[1*]

[1]Low Dimensional Materials Research Centre (LDMRC), Physics Department, Faculty of Science, University of Malaya, 50603 Kuala Lumpur, Malaysia

[2]Nanotechnology Laboratory, Esfarayen University, Esfarayen, North Khorasan, Iran

[3]Department of Chemistry, Faculty of Science, University Putra Malaysia, 43400 UPM Serdang, Selangor Darul Ehsan, Malaysia

[4]Photonics Research Centre, Physics Department, Faculty of Science, University of Malaya, 50603 Kuala Lumpur, Malaysia

[*]Corresponding authors: huangnayming@um.edu.my (Huang N.M) and amir_moradi_g@ymail.com (Moradi Golsheikh A.) Tel: +6012-2091008 Fax: +603-7967 4146

Abstract

Reduced graphene oxide (rGO) decorated with zinc sulphide nanospheres (ZnSNSs) was synthesized through the simple ultrasonic irradiation of an aqueous solution containing zinc acetate dihydrate ($Zn(CH_3COO)_2 \cdot 2H_2O$), thioacetamide ($C_2H_5NS$), and graphene oxide (GO). The results of X-ray diffraction, Fourier-transform infrared transmission spectroscopy, X-ray photoelectron spectroscopy and Raman spectroscopy confirmed the simultaneous formation of cubic-phase ZnSNSs and the reduction of GO through the ultrasonic irradiation process. Field emission scanning electron microscope images showed that the size and number density of the nanoparticles could be tuned by adjusting the precursor amounts. Transmission electron microscope images showed that the spherical ZnS nanoparticles were comprised of small nanoparticles with an average size of ~5 nm aggregated together. The result of

photoluminescence spectroscopy and Brunauer-Emmett-Teller (BET) measurement demonstrated that the incorporation of reduced graphene oxide (rGO) sheets with ZnSNSs suppressed the electron–hole recombination and increased the surface area of the composite. Hence, a significant enhancement in the photocatalytic degradation of methylene blue (MB) was observed with the ZnSNSs-rGO nanocomposite, compared to the bare ZnS particles.

1. Introduction

Over the past few decades, semiconductor nanostructures have attracted tremendous attention because of their unique physical and chemical properties and their potential photocatalyst,[1-3] energy conversion,[4-6] and chemical/biological sensing [7, 8] applications. Zinc sulphide (ZnS), as one of the first discovered and non-toxic II–VI semiconductors with a wide direct band gap (3.7 and 3.78 eV for a cubic zinc blend and hexagonal wurtzite structure, respectively),[9, 10] has been used for various applications such as electroluminescence, optical/electrochemical sensors, photocatalysts, and light-emitting diodes (LEDs).[11-16] At present, ZnS nanostructures have been prepared using a variety of techniques, including hydrothermal,[17] solvothermal,[18] sonochemical,[19] thermal evaporation,[20] chemical vapor deposition,[12] chemical deposition,[21] and chemical precipitation methods.[22]

Graphene, a one-atom-thick sheet of sp^2-bonded carbon atoms, with its high electrical conductivity, large surface-to-volume ratio, and excellent chemical tolerance is a good matrix for nanocomposite. Therefore, semiconductor-decorated graphene composites have been the focus of research in recent years because of their multifunctional abilities.[23, 24] It has been demonstrated that the charge-transferring and magnetic and electronic interactions between graphene sheets and the attached semiconductor nanostructures can improve their performance in various applications.[25-27] In a semiconductor, electrons can be exited from the valence band to

the conduction band by photons with the energy of *hv*, which is equal to or higher than the band gap energy of the semiconductor, resulting in the generation of electron–hole pairs. These electron–hole pairs play an important role in the photocatalytic degradation of pollutants and solar energy conversion. However, the photoexcited electrons in the conduction band and holes in the valence band are unstable and can easily recombine, which decreases their photocatalytic efficiency. The photoexcited electrons from the conduction band can be accepted by the graphene sheets incorporated into the semiconductor and suppress the recombination of electrons and holes. Moreover, graphene nanosheets assist in the growth and dispersion of nanoparticles on the semiconductor surface, which prevents the aggregation of the nanoparticles and produces a higher surface area for the photocatalyst.[28]

In recent years, a sonochemical strategy has been used for the synthesis of graphene-based inorganic nanocomposites such as metals,[29-31] bimetals,[32] metal oxides,[33-35] and metal sulphides.[36] The chemical effects of ultrasound irradiation arise from the acoustic cavitation phenomenon. When a liquid is irradiated with ultrasound, bubbles are created, and ultrasonic energy can accumulate with their growth and subsequent collapse, which leads to the release of the accumulated energy within a very short time. These cavitational implosions generate localized hotspots with a high temperature of 5000 K, pressure of 1000 bar, and heating and cooling rate of 10^{10} K/s.[37] These extreme conditions are suitable for reducing GO and metal ions. At present, ZnS-rGO nancomposite have been prepared using a variety of techniques, including hydrothermal,[14, 15] solvothermal [38, 39] and microwave assisted methods[40, 41], which are usually involved chemical reducing agents (such as gelatin,[14] ethylene glycol [39] and octylamine [41]) and/or surfactants (such as poly(acrylic acid) [39]). To the best of our knowledge, there has been no report on the sonochemical synthesis of ZnSNSs-rGO nanocomposites. Herein, we report for the

first time a fast, one-step, cost-effective, and environmentally friendly synthesis of rGO uniformly decorated with hierarchical ZnS nanospheres using a sonochemical method that does not involve chemical reduction and/or stabilizing agents.

2. Experimental

2.1. Materials

Graphite flakes (Ashbury Inc. (NJ, USA)) were used to synthesize graphene oxide (GO). Sulphuric acid (H_2SO_4, 98%), phosphoric acid (H_3PO_4, 85%), potassium permanganate ($KMnO_4$, 99.9%), hydrogen peroxide (H_2O_2, 30%), and hydrochloric acid (HCl, 37%) were purchased from Merck and used as received. Zinc acetate dehydrate ($Zn(CH_3COO)_2 \cdot 2H_2O$, ≥98.0%) and thioacetamide (CH_3CSNH_2, ≥99.0%) were purchased from Sigma-Alderich and used as received. Distilled water was used throughout the sample preparation.

2.2. Preparation of ZnSNSs-rGO nanocomposite

GO was prepared using a simplified Hummers' method.[42] To prepare the nanocomposite, 0.4, 0.8, 1.2, or 1.6 mM of an aqueous solution of zinc acetate dihydrate was added in a drop-wise fashion to 10 mL of an aqueous solution of GO (1.0 mg/mL) and stirred for 16 h (or overnight) to ensure the adsorbtion of the zinc ions to the surface of the GO sheets. Then, 0.4, 0.8, 1.2, or 1.6 mM of an aqueous solution of thioacetamide was added to the above mixture, and distilled water was used to achieve a final volume of 20 mL, which was stirred for 5 min to ensure homogeneity. The resulting solution was exposed to acoustic cavitation using an ultrasonic horn (Misonix Sonicator S-4000, USA, 20 kHz) immersed directly in the solution at an 80% amplitude for 15 min with a 3-s pulse and 3-s relaxation cycle. The products were centrifuged and washed with distilled water and ethanol several times, and finally dried at 60 °C for 24 h in a vacuum oven. The ultrasonic reaction was applied without any cooling. Thus, a

temperature of about 80 °C was reached after 15 min at the end of the reactions. For comparison, free ZnS particles were also synthesized using the same procedure with a solution of zinc acetate dihydrate and a solution of thioacetamide without GO.

2.3. Photocatalytic measurements

The photocatalytic degradation of methylene blue (MB) was carried out in order to evaluate the photocatalytic activity of the prepared ZnSNSs-rGO nanocomposites. Ten milligrams of the as-prepared ZnSNSs-rGO nanocomposite powder was dispersed in 50 mL of an aqueous solution of MB with an initial concentration of 10 mg/L. The above mixture was first stirred for 60 min in the dark to ensure that the adsorption-desorption equilibrium was reached. Then, the photocatalytic degradation reaction was carried out under the irradiation of UV lamps 8 cm above the solution (CL-1000 UV Crosslinkers; 5×8 W). After a given time interval during this UV irradiation, 3 mL of the suspension was collected and centrifuged. The UV–vis absorption spectra of the degraded solution supernatants were measured using a UV–visible spectrometer (Thermo Scientific Evolution), and the characteristic absorption peak of the MB solution at 663 nm was monitored.

3. Results and discussion

Figure 1 shows the XRD patterns of the pristine GO (a), sample holder (b), and ZnSNPs-rGO nanocomposites that were prepared using 2 mL of the solution of zinc acetate dihydrate (2M) at different ultrasonic irradiation times (c–e) (5, 15, and 30 min, respectively). The pristine GO has a sharp peak at 10.8°, which is assigned to the (002) inter-planar spacing of 0.82 nm.[43] Meanwhile, the XRD pattern of the sample holder has a broad peak at about 2θ = 13°, which is observed in the XRD patterns of all the samples. As shown in Figure 1c, after 5 min of ultrasonic

irradiation, a broad peak appears at 28.85°, which indicates the formation of ZnS particles in the composite. When the ultrasonic irradiation time increases to 15 min, in addition to the broad peak at 28.85°, two small broad peaks appear at 48.1° and 56.75°, which indicate the crystal growth of ZnS particles. All of the peaks at 28.85°, 48.1°, and 56.75° can be indexed to the (111), (220), and (311) planes of the cubic ZnS (PDF card no: 00-065-0309). The calculated lattice spaces of the (111), (220), and (311) planes are 3.09, 1.89, and 1.62 Å, respectively. When the ultrasonic irradiation time was increased to 30 min, the intensity of the peaks did not change significantly. Meanwhile, the (002) peak of GO disappeared after the sonication process. This is attributed to the growth of ZnS particles on the surface of the graphene sheets during the ultrasonication process, which led to the exfoliation of the GO sheets and prevented the restacking of the graphene sheets.

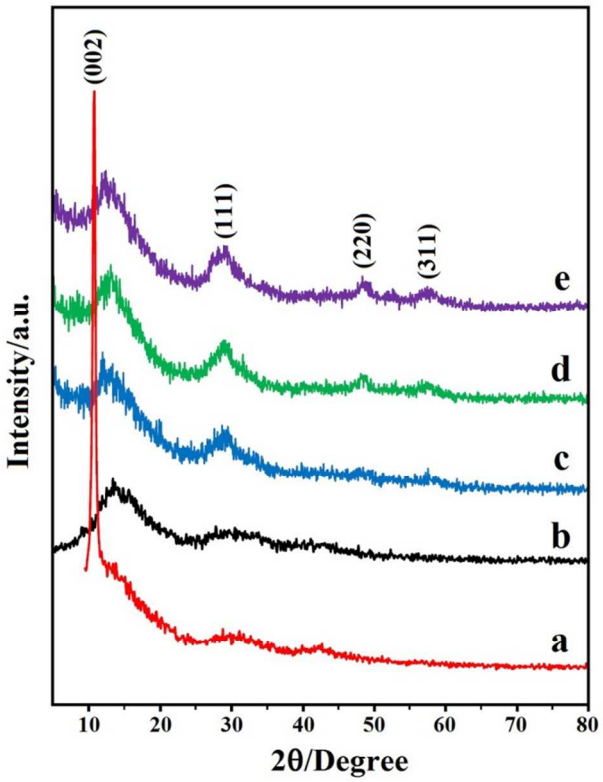

Figure 1 XRD patterns of pristine GO (a), sample holder (b), and ZnSNSs-rGO nanocomposites prepared using different ultrasonic irradiation times: 5 min (c), 15 min (d), and 30 min (e).

Figure 2 shows the FTIR spectra of the pristine GO (a) and ZnSNSs-rGO nanocomposite (b). For GO, the broad peak centered at 3233 cm^{-1} is attributed to the O-H stretching vibrations, while the peaks at 1739, 1627, 1395, and 1226 are assigned to the C=O stretching, sp^2-hybridized C=C group and O-H bending, C-OH stretching, and C-O-C stretching, respectively.[44] In addition, the peaks at 1170 and 1047 cm^{-1} can be attributed to the C-O vibration of the epoxy or alkoxy groups.[45] For the ZnSNSs-rGO nanocomposite, the peak at 1556 cm^{-1} is assigned to the sp^2-hybridized C=C group. The peak at 1739 cm^{-1} for GO is absent for the ZnS/rGO nanocomposite, and the intensity of the peaks related to the oxygen-containing groups decreases for the ZnSNSs-rGO nanocomposites, which indicates the reduction of GO during the ultrasonic irradiation process. The inset of Figure 2 shows a photograph of the solution of GO, zinc acetate dehydrate, and thioacetamide before and after the ultrasonic irradiation treatment. The color changed from yellow brown to black, and the resultant precipitated in water, which indicated the effective reduction of GO.

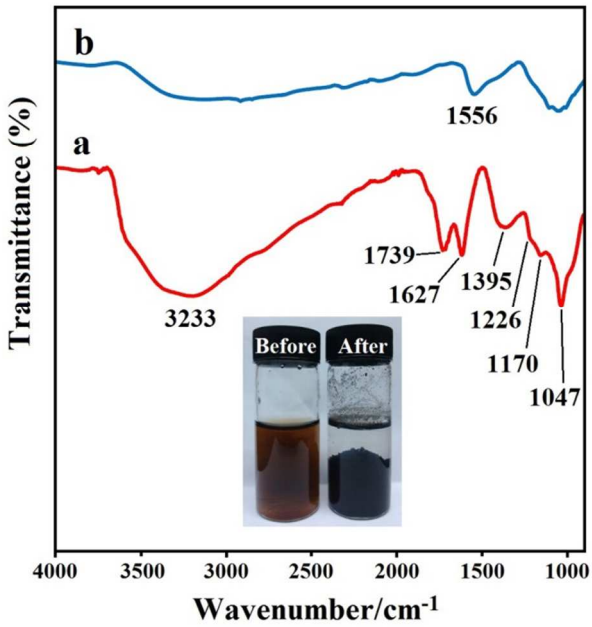

Figure 2 FTIR spectra of pristine GO (a) and ZnSNSs-rGO nanocomposite (b). Inset shows photograph of solution of GO, zinc acetate dehydrate, and thioacetamide before and after ultrasonic irradiation.

The XPS spectra further proved the reduction of GO and the formation of ZnS after ultrasonic treatment, as shown in Figure 3. As shown in Figure 3a, the C 1s band of pristine GO can be fitted to four deconvulated components, centred at 284.5, 285.4, 286.2, 287.8 and 289 eV, which are assigned to the C=C sp^2 bonds in the graphitic network, carbon bonds with sp^3 hybridization, the C in C-O, the C in C=O and the C in C(O)O, respectively.[46, 47] In comparison to the pristine GO, the C 1s band of the ZnSNPs-rGO composite shows that the peak intensity of the oxygenated carbonaceous bands decreased, indicating the reduction of GO after ultrasonic treatment. As shown in Figure 3c, the Zn 2p core level spectrum for ZnSNPs-rGO composite shows the two peaks at 1020.6 and 1043.6 eV, which are attributed to the Zn $2p_{3/2}$ and Zn $2p_{1/2}$, respectively.[48] The spin–orbit splitting of Zn $2p_{1/2}$ and Zn $2p_{3/2}$ is 23.0 eV, which is characteristic of ZnS.[49] Moreover, the S 2p core level spectrum for ZnSNPs-rGO contains the two peaks at

160.3 and 161.1 eV with a peak separation of 0.8 eV, which are assigned to the S $2p_{3/2}$ and S $2p_{1/2}$, respectively.[48, 50]

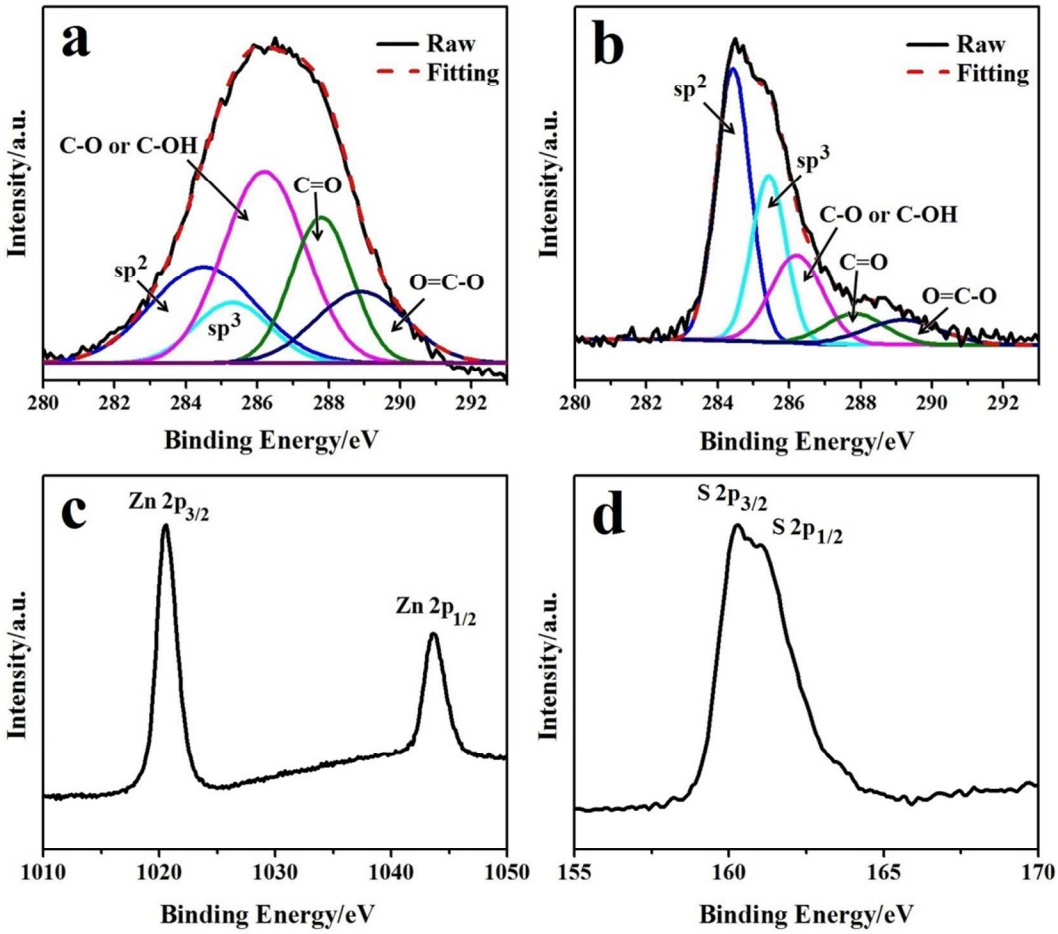

Figure 3 High resolution XPS spectra of pristine GO for C1s core level (a) and ZnSNPs-rGO for: (b) C1s core level, (c) Zn2p core level and (d) S2p core level.

Figure 4 shows the Raman spectra for the pristine GO (a) and ZnSNSs-rGO nanocomposite (b). The Raman spectra of GO shows two peaks at 1350 and 1608 cm^{-1}, which correspond to the well-known D and G bands, respectively. The D band is assigned to the breathing mode of the A_{1g} symmetry involving phonons near the K-zone boundary. Meanwhile, the G band is assigned to the E_{2g} mode of sp^2-bonded carbon atoms.[51] In comparison to the

pristine GO, the Raman spectra of the ZnSNSs-rGO nanocomposite shows that the D and G bands shifted to lower wave numbers at 1344 and 1600 cm^{-1}, respectively. This was because of the reduction of GO during the ultrasonic irradiation process.[52, 53] Moreover, Figure 3 shows that the I (D)/I (G) intensity ratio of the ZnSNSs-rGO nanocomposite increased to a slightly higher value of 1.04 compared to that of GO (0.92), which indicated the formation of a larger number of in-plane sp^2 domains with a smaller average size.

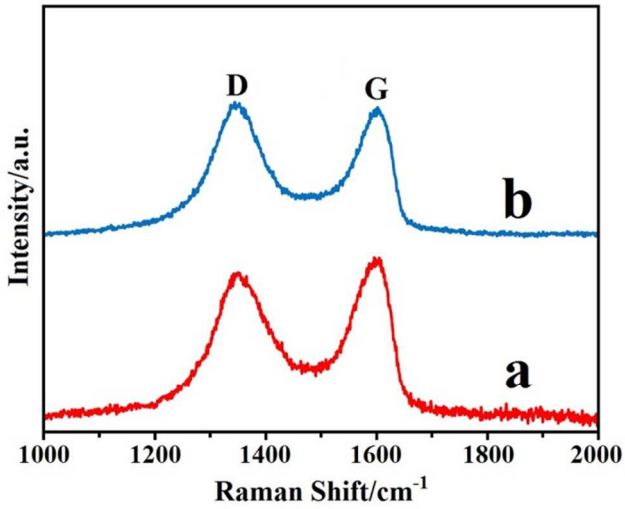

Figure 4 Raman spectra of pristine GO (a) and ZnSNSs-rGO nanocomposite (b).

Figure 5 illustrates the representative FESEM images and size distribution diagrams of the ZnSNSs-rGO nanocomposites prepared using the solution with GO (1.0 mg/mL) and different amounts of zinc acetate dehydrate: 0.4 mM (a and b), 0.8 mM (c and d), 1.2 mM (e and f), and 1.6 mM (g and h), and ZnS particles (i and j). When 0.4 mM of zinc acetate was used for preparing the nanocomposite, as shown in Figure 5a and 5b, ZnS nanospheres with a mean size of 33.3 nm and a low number density were generated on the surface of the reduced graphene oxide because of the large number of residual oxygen containing groups on the surface of the GO. In addition, Figure 5a shows that some of the ZnS nanospheres were out of focus, indicating that the ZnS nanospheres were located on both sides of the rGO sheets, and the rGO sheets were

rough because of wrinkles, or they were located on the surface of the bottom layer rGO sheets. As shown in Figure 5, when the amount of zinc acetate increases from 0.4 mM to 1.2 mM, the mean size of the ZnS nanospheres is increases slightly from 33.3 nm to 40.5 nm, but their number density increases significantly. This is because the Zn^{2+} ions prefer to adsorb onto the surface of GO and produce new initial nucleation sites because of the sufficient number of residual oxygen containing groups on the surface of the GO nanosheets, instead of absorption to the preformed ZnS nanospheres to form larger ZnS nanospheres. By further increasing the zinc acetate to 1.6 mM, the average size of the ZnS nanospheres is increased significantly, which indicates the absorption of the excess Zn^{2+} ions to the preformed ZnS nanoparticles to form larger nanoparticles as a result of the smaller number of free residual oxygen containing groups. As shown in Figure 5i and 5j, ZnS particles with a mean size of 142.4 nm were obtained and stacked together randomly in the absence of GO. This indicated that graphene nanosheets play an important role in assisting the growth and dispersion of ZnS nanospheres on their surface, which prevents the aggregation of ZnS nanospheres.

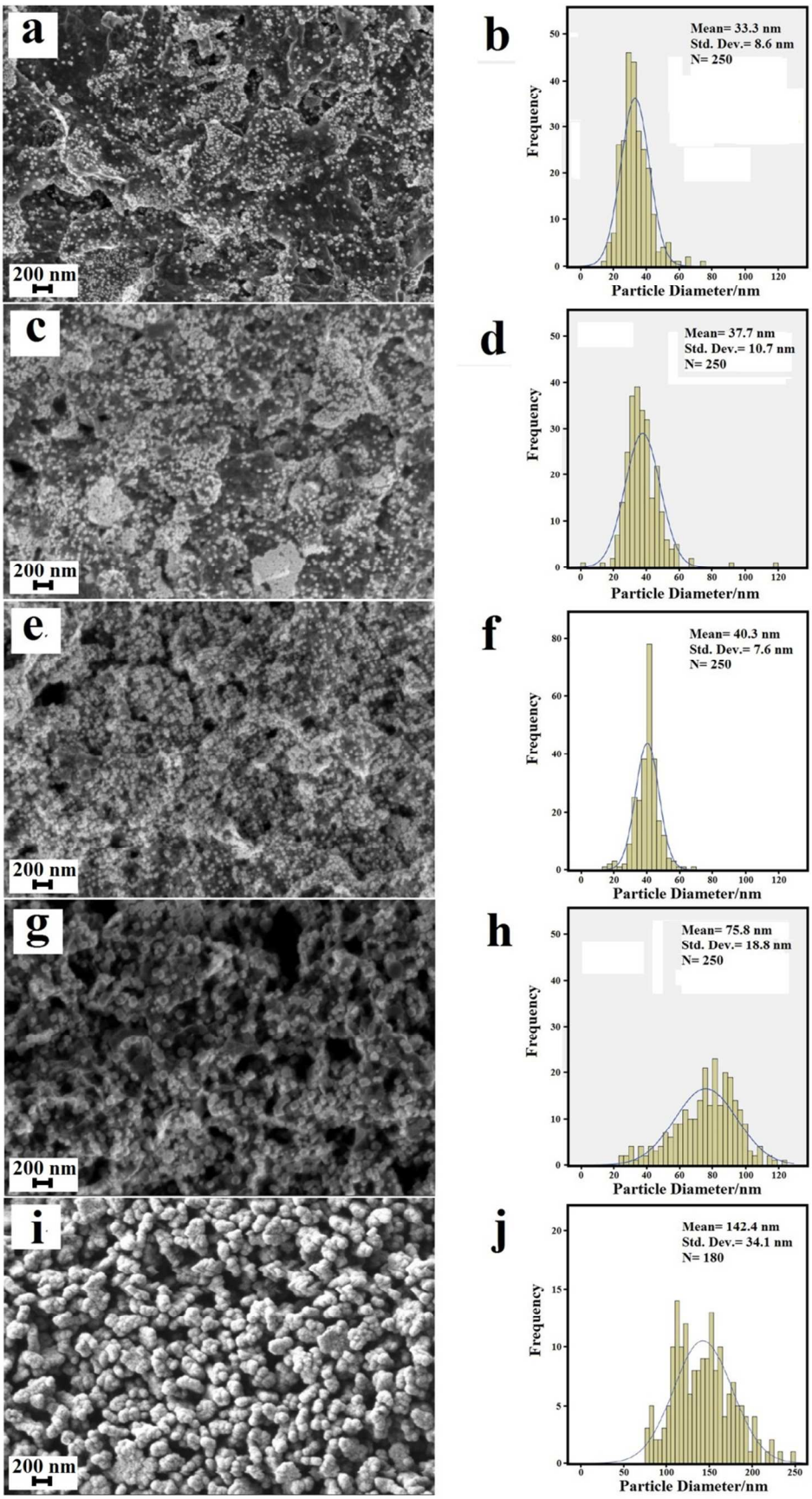

Figure 5 FESEM images and size distribution diagrams of ZnSNSs-rGO nanocomposites prepared using solution with GO (1.0 mg/mL) and different amounts of zinc acetate dehydrate: 0.4 mM (a and b), 0.8 mM (c and d), 1.2 mM (e and f), and 1.6 mM (g and h), and ZnS particles (i and j).

The structure of the ZnSNSs-rGO nanocomposite was further analyzed using HRTEM. Figure 6 shows low- and high-resolution TEM images of the ZnSNSs-rGO nanocomposite. A graphene sheet can be clearly observed with typical wrinkles, with ZnS nanoparticles with a spherical shape anchored on its surface. Figure 6b shows that the spherical ZnS nanoparticles are comprised of many small nanoparticles with an average size of ~5 nm aggregated together. Figure 6c shows an HRTEM image of a ZnS nanosphere anchored to the surface of an rGO sheet. The measured lattice fringe spaces of 0.31 and 0.19 nm are attributed to the (111) and (220) planes of ZnS, respectively, which is in agreement with the XRD results.

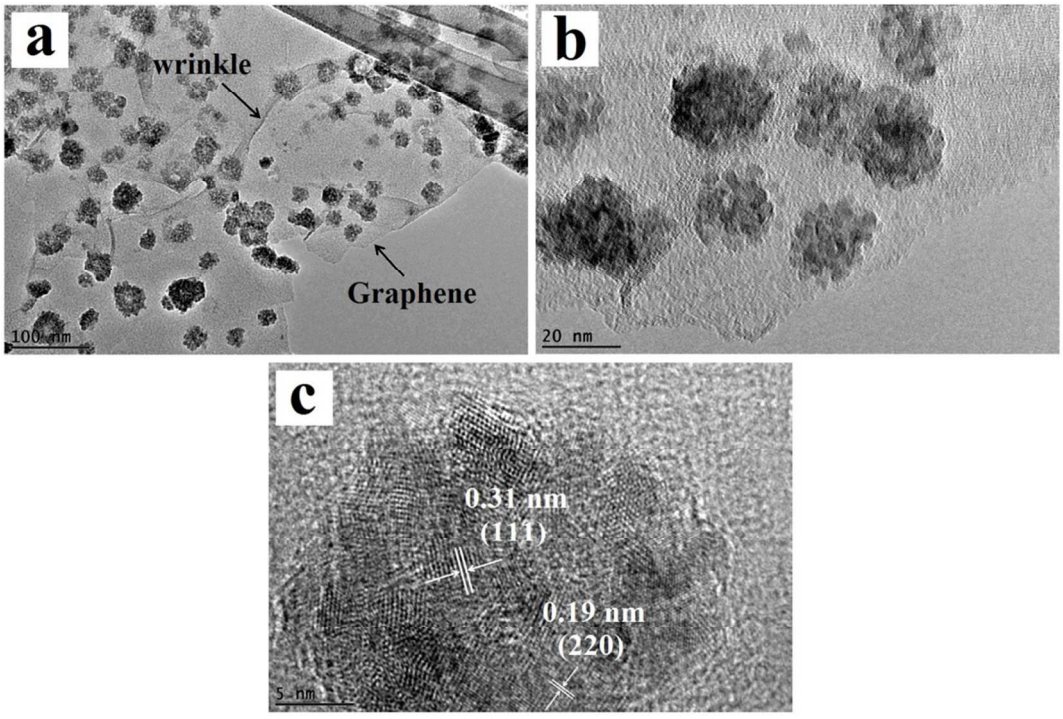

Figure 6 TEM images of ZnSNSs-rGO nanocomposite at different magnifications.

The surface area and porous nature of the ZnS and ZnSNSs-rGO nanocomposite was further evaluated by measuring the nitrogen adsorption–desorption isotherms as shown in Figure 7. According to the International Union of Pure and Applied Chemistry (IUPAC) classification, the nitrogen adsorption–desorption isotherms of both exhibited the characteristic of type-IV isotherms, which indicates the mesoporous nature of them (see Figure 7a).[38, 54] The measured BET surface areas for ZnS and ZnSNSs-rGO nanocomposite are 5.14 and 66.81 m^2/g, respectively. Figure 7b shows the Barrett–Joyner–Halenda (BJH) pore size distribution curve of ZnS and ZnSNSs-rGO nanocomposite. As shown in Figure 7b, the pore size distribution exhibits a peak at 2.3 nm for ZnSNSs-rGO nanocomposite and a braod peak with a maximum at 10.5 nm for ZnS, which indicates the mesoporous nature of the ZnS and ZnSNSs-rGO nanocomposite. The total volume of pores for ZnS and ZnSNSs-rGO nanocomposite were 0.0059 and 0.2478 cm^3/g, respectively. The high BET surface area and large total volume of pores for the ZnSNSs-rGO nanocomposite compared to the ZnS are due to high theoretical specific surface area of graphene (2600 m^2/g).

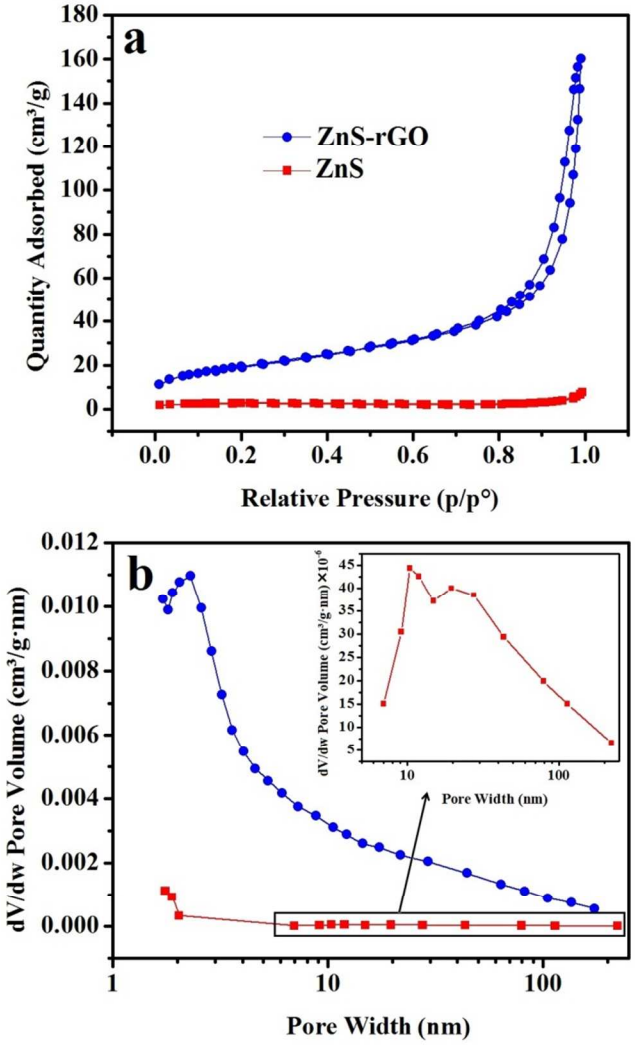

Figure 7 (a) Nitrogen adsorption–desorption isotherms of ZnS and ZnSNSs-rGO nanocomposite, and (b) BJH pore-size distribution of ZnS and ZnSNSs-rGO nanocomposite. The inset highlights the pore-size distribution peaks of ZnS.

The formation mechanism of the ZnSNSs-rGO *via* a sonochemical reaction is shown in Figure 8. GO sheets dispersed in water are negatively charged as a result of the ionization of the carboxyl and hydroxyl groups on the surface of the GO (Figure 8a).[55] This causes the positively charged Zn^{2+} ions to be adsorbed on the negatively charged GO sheets by electrostatic attraction (Figure 8b). When an aqueous solution is irradiated with ultrasound, bubbles are created, and ultrasonic energy accumulates during their growth. The rapid collapse of these bubbles leads to

the creation of localized hotspots with a high temperature of 5000 K, pressure of 1000 bar, and heating and cooling rate of 10^{10} K/s. Under these conditions, highly reactive H and OH radicals can be generated by the pyrolysis of water molecules.[37]

$$H_2O))))))\ H^{\bullet} + OH^{\bullet} \quad (1)$$

The generated $H^{\bullet}$ radicals can react with thioacetamide to produce H_2S.[56]

$$H^{\bullet} + OH^{\bullet} + CH_3CSNH_2 \rightarrow CH_3C(NH_2)(OH)\text{-}SH \quad (2)$$

Repeating this process would then result in the formation of $CH_3C(NH_2)(OH)_2$ (which would immediately lose water to give CH_3CONH_2) and H_2S.

$$H^{\bullet} + OH^{\bullet} + CH_3C(NH_2)(OH)\text{-}SH \rightarrow CH_3C(NH_2)(OH)_2 + H_2S \quad (3)$$

The formation of H_2S may also follow another route as well.[19, 56, 57]

$$CH_3CSNH_2 + 2H^{\bullet} \rightarrow H_2S + {}^{\bullet}C(NH_2)CH_3 \quad (4)$$

Then the generated H_2S reacts with Zn^{2+} ions to yield ZnS.

$$Zn^{2+} + H_2S \rightarrow ZnS + 2H^{+} \quad (5)$$

The generated $H^{\bullet}$ and $R^{\bullet}$ (${}^{\bullet}C(NH_2)CH_3$) radicals act as reducing species, resulting in the reduction of GO:[29]

$$GO + \text{reducing species } (H^{\bullet}, R^{\bullet}) \rightarrow rGO \quad (6)$$

In addition, GO is a thermally unstable material above 200 °C. Hence, the high temperature generated during ultrasonic irradiation could reduce GO to graphene.[58] When the concentration of zinc acetate increases, the free Zn^{2+} ions in the aqueous solution continue to grow on the previously formed ZnSNPs, as well as nucleating on the rGO sheets, which explains the increased particle size and density on the rGO sheets.

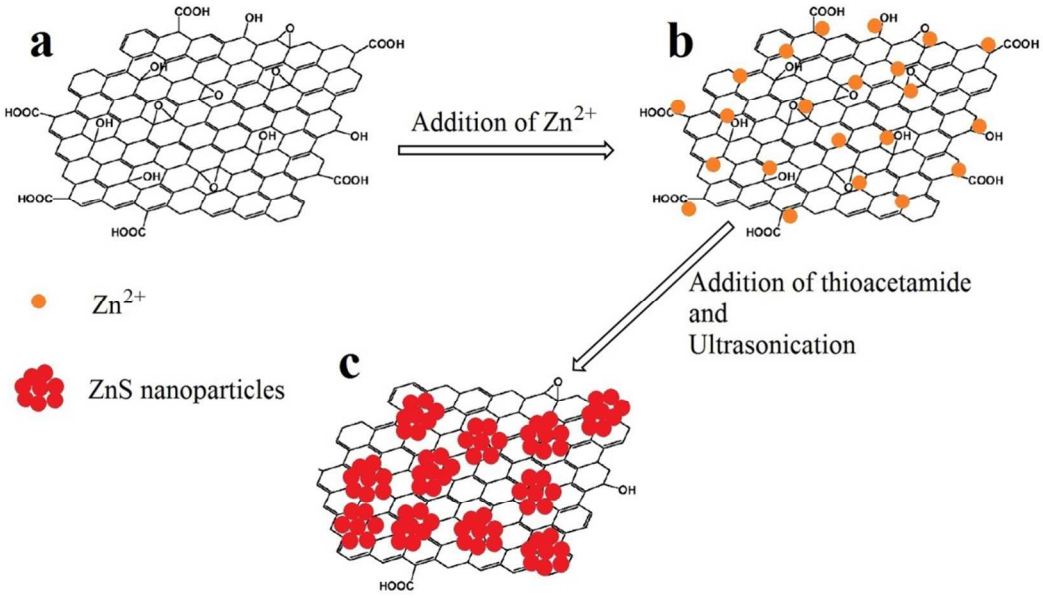

Figure 8 Schematic illustration of formation mechanism for ZnSNPs-rGO composite via ultrasonic irradiation.

Figure 9A shows the room temperature photoluminescence spectra of the ZnS particles (a) and ZnSNSs-rGO nanocomposite (b). The photoluminescence spectrum of the ZnS particles exhibits weak shoulders around 416 and 445 nm, and broad peaks at 540 and 575 nm. These shoulders and peaks may be related to the point defects, which can serve as luminescent sites. The point defects, which can be presented in ZnS particles, are sulfur vacancies, zinc vacancies, interstitial sulfur atoms, and interstitial zinc atoms. The blue emission shoulders at 416 and 445 nm are attributed to transitions from the conduction band to the energy level of interstitial sulfur atoms and zinc vacancies, respectively.[59] The green emission peak at 540 nm can be attributed to the transition between the energy level of sulfur vacancies and interstitial sulfur atoms.[60] The orange emission peak at 575 nm could be associated with the transition between the energy level of interstitial zinc atoms and zinc vacancies. The photoluminescence spectrum of the ZnSNSs-rGO nanocomposite demonstrates that after the incorporation of ZnS nanoparticles with graphene sheets, the photoluminescence emission of the ZnS nanoparticles was significantly

quenched. This indicates that after the incorporation, the photogenerated electron–hole pairs in the ZnS nanospheres could be efficiently separated through the transfer of electrons from the conduction band of the ZnS nanospheres (-3.65 eV *vs.* vacuum) to the rGO sheets (with a work function of about -4.42 eV *vs.* vacuum), which suppressed the electron–hole recombination (as shown in Figure 9B).

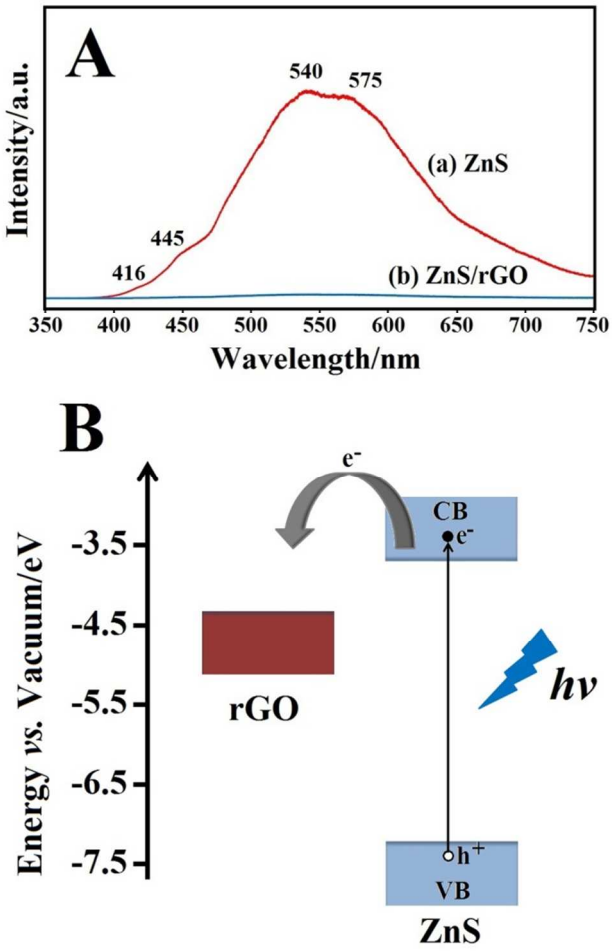

Figure 9 (A) Room temperature photoluminescence spectra of pure ZnS (a) and ZnSNSs-rGO nanocomposite (b), (B) Energy level diagram of ZnSNSs-rGO nanocomposite.

The photocatalytic activities of the ZnS particles and ZnSNSs-rGO nanocomposites were measured using the liquid-phase degradation of MB under UV irradiation at ambient temperature. Figure 10a illustrates the absorption spectra of the MB aqueous solution in the

presence of the ZnSNSs-rGO-1.2 nanocomposite under UV light irradiation for different time intervals. It can easily be observed that the intensity of the absorption peak of the MB at 663 nm decreases with an increase in the UV light irradiation time, which indicates the degradation of MB molecules by the photocatalytic phenomena. Figure 10b shows a comparison of the photocatalytic activities of pure ZnS particles and ZnSNSs-rGO nanocomposites prepared with different amounts of zinc acetate dehydrate as the precursor of zinc ions. As can be seen in Figure 8b, pure ZnS particles have a low photocatalytic activity in comparison with the ZnSNSs-rGO nanocomposites. The high photocatalytic activity of the composites could be explained by the following causes. MB molecules can be adsorbed onto the surface of graphene with an offset face-to-face orientation *via* π-π conjugation between MB and the aromatic regions of graphene, which increases the adsorptivity of MB compared to the bare ZnS and is an important prerequisite to obtain a good photocatalytic activity.[61] To show the effect of the graphene on the adsorption of MB in the composite, the UV–vis absorption spectrum of MB under a dark condition was monitored, as shown in Figure 11. It can easily be seen after equilibrium in the dark for 15 min that most of the MB molecules (ca. 90%) remained in the solution with pure ZnS as the catalyst, whereas a large number of MB molecules were adsorbed on the surface of the ZnSNSs-rGO nanocomposites. Meanwhile, Figure 11 shows that the adsorption of MB molecules increases with an increase in the graphene in the composite. In general, when a semiconductor is illuminated with photons, electrons in the valance band of the semiconductor are excited into the conduction band, resulting in the generation of electron–hole pairs. These electron–hole pairs either recombine or migrate to the surface of the photocatalyst to initiate a series of photocatalytic reactions and produce hydroxyl radicals, $^{\bullet}OH$ and superoxide radicals, $^{\bullet}O_2^-$ in water, resulting in the degradation of organic pollutants. It is found $^{\bullet}OH$ has a major

contribution during the photocatalytic degradation of the dye. For ZnS, the generation of $^{\bullet}OH$ mainly comes from $^{\bullet}O_2^-$ due to its valence band position is less positive than that of the $OH^-/^{\bullet}OH$ couple.[38, 62] The generation of $^{\bullet}OH$ in ZnS is low due to rapid electron-hole recombination. In the ZnSNSs-rGO nanocomposites, as discussed in a photoluminescence study, graphene can trap the photogenerated electrons from the conduction band of ZnS and transfer them through its surface, which suppresses the electron–hole recombination and promoted the formation of $^{\bullet}OH$ based on the following reactions:[38]

$$ZnS + h\nu \rightarrow ZnS\ (e^- + h^+) \quad (7)$$

$$ZnS\ (e^- + h^+) + Graphene \rightarrow ZnS\ (h^+) + Graphene\ (e^-) \quad (8)$$

$$Graphene\ (e^-) + O_2 \rightarrow Graphene + {}^{\bullet}O_2^- \quad (9)$$

$${}^{\bullet}O_2^- + 2H^+ + e^- \rightarrow H_2O_2 \quad (10)$$

$$H_2O_2 + e^- \rightarrow {}^{\bullet}OH + OH^- \quad (11)$$

Although, the valence band position of ZnS is less positive than that of the $OH^-/^{\bullet}OH$ couple, the generation of $^{\bullet}OH$ can be occur in the valence band by the following reaction:[38, 40]

$$ZnS\ (h^+) + OH^- \rightarrow ZnS + {}^{\bullet}OH \quad (12)$$

The generated $^{\bullet}OH$ either from conduction band or valence band can degrade the MB.[25]

$$^{\bullet}OH + Pollutants \rightarrow Degradation\ products\ (such\ as\ CO_2\ and\ H_2O) \quad (13)$$

Finally, the size of the ZnS particles in the composites was smaller than the pure ZnS particles, leading to a higher surface area for the photocatalyst and thus improving the photocatalytic activity of the ZnSNSs-rGO nanocomposite.

In addition, the photocatalytic activity of the ZnSNSs-rGO nanocomposite increased with an increase in the initial amount of zinc acetate dehydrate, which was used as a precursor for zinc ions, from 0.4 to 1.2 mM. It is plausible that this occurred because the amount of ZnS increased

in the composite, resulting in an increase in the photogenerated electron–hole pairs. A further increase in the initial amount of zinc acetate dehydrates to 1.6 mM led to a decrease in the photocatalytic activity of the ZnSNSs-rGO nanocomposite. This may have been due to the fact that the size of the ZnS nanoparticles increased, which decreased the active surface area of the nanoparticles and therefore decreased the photocatalytic activity.

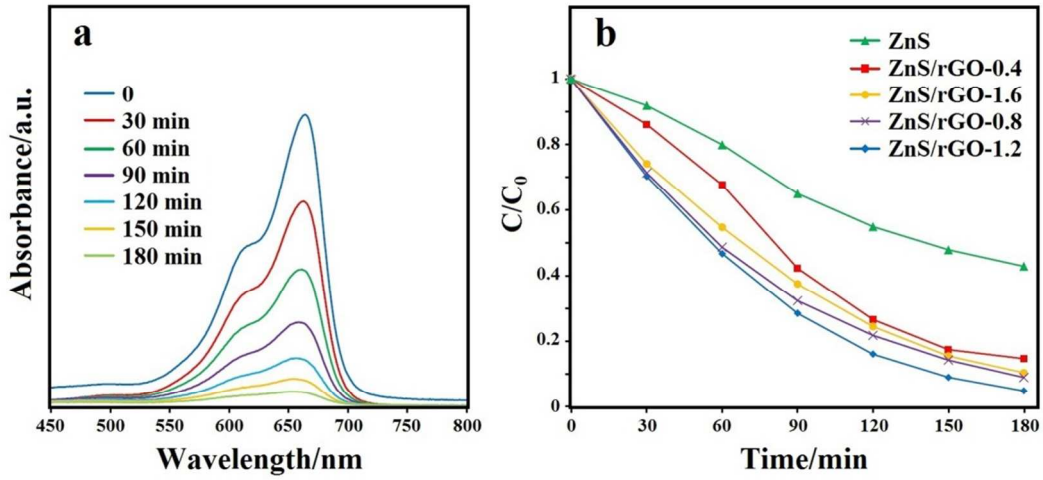

Figure 10 Photocatalytic activities: (a) UV–vis absorption spectra of MB aqueous solution at different times in presence of ZnSNSs-rGO-1.2 as photocatalyst and (b) photodegradation rate of MB at different time intervals in presence of various photocatalysts.

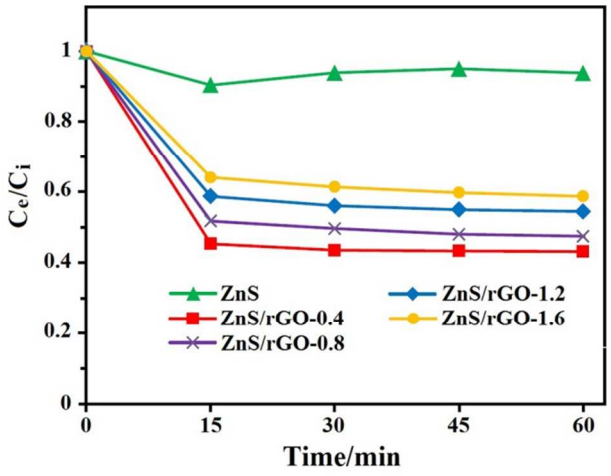

Figure 11 Adsorption-desorption equilibrium rate of MB under dark condition versus time in the presence of various photocatalysts.

4. Conclusion

rGO decorated with zinc sulphide nanoparticles (ZnSNPs) was successfully synthesized using a one-pot sonochemical synthesis method without using any stabilizing, capping, or reducing agents. The particle size and number density of the ZnSNPs anchored on the surface of the rGO sheets could be easily tuned by adjusting the amounts of the precursors. It was established that the reduced graphene oxide sheets played important roles in enhancing the photocatalytic efficiency of the ZnSNPs-rGO nanocomposite, as compared to the bare ZnS, which can be as follows: 1) the prevention of the ZnSNPs agglomeration, leading to the growth of small nanoparticles on its surface and achieving a higher active surface area, 2) the increasing of the adsorption of MB molecules, and 3) the suppression of electron–hole recombination.

Acknowledgement

This work was supported by a UMRG Program Grant (RP007C/13AFR) from the University of Malaya and a High Impact Research Grant from the Ministry of Higher Education of Malaysia (UM.C/625/1/HIR/MOHE/SC/21).

References

1. M. R. Hoffmann, S. T. Martin, W. Choi and D. W. Bahnemann, *Chem. Rev.*, 1995, 95, 69-96.
2. J. S. Lee and J. Jang, *J. Ind. and Eng. Chem.*, 2014, 20, 363-371.
3. H. Kisch, *Angew. Chem. Int. Ed.*, 2013, 52, 812-847.
4. K. Rajeshwar, *J. Phys. Chem. Lett.*, 2011, 2, 1301-1309.

5. S. T. Kochuveedu, Y. H. Jang and D. H. Kim, *Chem. Soc. Rev.*, 2013, 42, 8467-8493.

6. T. Miyasaka, *Electrochemistry*, 2010, 78, 960-969.

7. Y. Lou, Y. Zhao, J. Chen and J.-J. Zhu, *J. Mater. Chem. C*, 2014, 2, 595-613.

8. R. Freeman and I. Willner, *Chem. Soc. Rev.*, 2012, 41, 4067-4085.

9. T. Trindade, P. O'Brien and N. L. Pickett, *Chem. Mater.*, 2001, 13, 3843-3858.

10. X. Fang, T. Zhai, U. K. Gautam, L. Li, L. Wu, Y. Bando and D. Golberg, *Prog. Mater. Sci.*, 2011, 56, 175-287.

11. E. Schlam, *P. IEEE*, 1973, 61, 894-901.

12. X. Fang, Y. Bando, M. Liao, U. K. Gautam, C. Zhi, B. Dierre, B. Liu, T. Zhai, T. Sekiguchi, Y. Koide and D. Golberg, *Adv. Mater.*, 2009, 21, 2034-2039.

13. M. H. Mashhadizadeh and E. Afshar, *Electroanal.*, 2012, 24, 2193-2202.

14. Y. Feng, N. Feng, G. Zhang and G. Du, *CrystEngComm*, 2014, 16, 214-222.

15. M. Sookhakian, Y. M. Amin and W. J. Basirun, *Appl. Surf. Sci.*, 2013, 283, 668-677.

16. J. Ziegler, S. Xu, E. Kucur, F. Meister, M. Batentschuk, F. Gindele and T. Nann, *Adv. Mater.*, 2008, 20, 4068-4073.

17. C. Liu, Y. Ji and T. Tan, *J. Alloy. Compd.*, 2013, 570, 23-27.

18. S. Biswas, S. Kar and S. Chaudhuri, *J. Phys. Chem. B*, 2005, 109, 17526-17530.

19. N. A. Dhas, A. Zaban and A. Gedanken, *Chem. Mater.*, 1999, 11, 806-813.

20. S. Kar and S. Chaudhuri, *J. Phys. Chem. B*, 2005, 109, 3298-3302.

21. S. Biswas, P. Pramanik and P. K. Basu, *Mater. Lett.*, 1986, 4, 81-84.

22. R. Chauhan, A. Kumar and R. P. Chaudhary, *Spectrochim. Acta A*, 2013, 113, 250-256.

23. A. M. Golsheikh, N. M. Huang, H. N. Lim, C. H. Chia, I. Harrison and M. R. Muhamad, *Chem. Eng. J.*, 2013, 218, 276-284.

24. S. Bai and X. Shen, *RSC Adv.*, 2012, 2, 64-98.

25. Q. Xiang, J. Yu and M. Jaroniec, *Chem. Soc. Rev.*, 2012, 41, 782-796.

26. P. V. Kamat, *J Phys. Chem. Lett.*, 2009, 1, 520-527.

27. Q. Xiang and J. Yu, *J. Phys. Chem. Lett.*, 2013, 4, 753-759.

28. J. Qu, L. Shi, C. He, F. Gao, B. Li, Q. Zhou, H. Hu, G. Shao, X. Wang and J. Qiu, *Carbon*, 2014, 66, 485-492.

29. K. Vinodgopal, B. Neppolian, I. V. Lightcap, F. Grieser, M. Ashokkumar and P. V. Kamat, *J. Phys. Chem. Lett.*, 2010, 1, 1987-1993.

30. S. Chandra, S. Bag, R. Bhar and P. Pramanik, *J. Nanopart. Res.*, 2011, 13, 2769-2777.

31. A. M. Golsheikh, N. M. Huang, H. N. Lim and R. Zakaria, *RSC Adv.*, 2014, 4, 36401-36411.

32. S. Anandan, A. Manivel and M. Ashokkumar, *Fuel Cells*, 2012, 12, 956-962.

33. G. Park, L. Bartolome, K. G. Lee, S. J. Lee, D. H. Kim and T. J. Park, *Nanoscale*, 2012, 4, 3879-3885.

34. S. Zhu, J. Guo, J. Dong, Z. Cui, T. Lu, C. Zhu, D. Zhang and J. Ma, *Ultrason. Sonochem.*, 2013, 20, 872-880.

35. A. Abulizi, G.-H. Yang and J.-J. Zhu, *Ultrason. Sonochem.*, 2014, 21, 129-135.

36. J. Shi, X. Zhou, Y. Liu, Q. Su, J. Zhang and G. Du, *Mater. Lett.*, 2014, 126, 220-223.

37. J. H. Bang and K. S. Suslick, *Adv. Mater.*, 2010, 22, 1039-1059.

38. L. Yu, H. Ruan, Y. Zheng and D. Li, *Nanotechnology*, 2013, 24, 375601.

39. P. Wang, T. Jiang, C. Zhu, Y. Zhai, D. Wang and S. Dong, *Nano Res.*, 2010, 3, 794-799.

40. H. Hu, X. Wang, F. Liu, J. Wang and C. Xu, *Synthetic Met.*, 2011, 161, 404-410.

41. Z. Bin, C. Xiaohua, T. Qianxiang, C. Chuansheng and H. Aiping, *Appl. Surf. Sci.*, 2014, 308, 321-327.

42. N. M. Huang, H. N. Lim, C. H. Chia, M. A. Yarmo and M. R. Muhamad, *Int. J. Nanomed.*, 2011, 6, 3443-3448.

43. G. Xie, J. Cheng, Y. Li, P. Xi, F. Chen, H. Liu, F. Hou, Y. Shi, L. Huang, Z. Xu, D. Bai and Z. Zeng, *J. Mater. Chem.*, 2012, 22, 9308-9314.

44. C. Cheng, S. Nie, S. Li, H. Peng, H. Yang, L. Ma, S. Sun and C. Zhao, *J. Mater. Chem. B*, 2013.

45. V. H. Pham, T. V. Cuong, S. H. Hur, E. Oh, E. J. Kim, E. W. Shin and J. S. Chung, *J. Mater. Chem.*, 2011, 21, 3371-3377.

46. A. Siokou, F. Ravani, S. Karakalos, O. Frank, M. Kalbac and C. Galiotis, *Appl. Surf. Sci.*, 2011, 257, 9785-9790.

47. D. R. Dreyer, S. Park, C. W. Bielawski and R. S. Ruoff, *Chem. Soc. Rev.*, 2010, 39, 228-240.

48. S. K. Apte, S. N. Garaje, S. S. Arbuj, B. B. Kale, J. O. Baeg, U. P. Mulik, S. D. Naik, D. P. Amalnerkar and S. W. Gosavi, *J. Mater. Chem.*, 2011, 21, 19241-19248.

49. S. A. Acharya, N. Maheshwari, L. Tatikondewar, A. Kshirsagar and S. K. Kulkarni, *Cryst. Growth Des.*, 2013, 13, 1369-1376.

50. J. Wang, Y.-F. Lim and G. Wei Ho, *Nanoscale*, 2014, 6, 9673-9680.

51. A. C. Ferrari and J. Robertson, *Phys. Rev. B*, 2000, 61, 14095-14107.

52. T. N. Lambert, C. A. Chavez, B. Hernandez-Sanchez, P. Lu, N. S. Bell, A. Ambrosini, T. Friedman, T. J. Boyle, D. R. Wheeler and D. L. Huber, *J. Phys. Chem. C*, 2009, 113, 19812-19823.

53. X. Liu, L. Pan, Q. Zhao, T. Lv, G. Zhu, T. Chen, T. Lu, Z. Sun and C. Sun, *Chem. Eng. J.*, 2012, 183, 238-243.

54. K. S. W. Sing, D. H. Everett, R. A. W. Haul, L. Moscou, R. A. Pierotti, J. Rouqu´erol and T. Siemieniewska, *Pure Appl. Chem.*, 1985, vol. 57, p. 603.

55. D. Li, M. B. Muller, S. Gilje, R. B. Kaner and G. G. Wallace, *Nat. Nano*, 2008, 3, 101-105.

56. H. Wang, J.-J. Zhu, J.-M. Zhu and H.-Y. Chen, *J.Phys.Chem. B*, 2002, 106, 3848-3854.

57. J. Z. Sostaric, R. A. Caruso-Hobson, P. Mulvaney and F. Grieser, *J. Chem. Soc. Farad. T.*, 1997, 93, 1791-1795.

58. K. Krishnamoorthy, G.-S. Kim and S. J. Kim, *Ultrason. Sonochem.*, 2013, 20, 644-649.

59. D. Denzler, M. Olschewski and K. Sattler, *J. Appl. Phys.*, 1998, 84, 2841-2845.

60. X. Wang, J. Shi, Z. Feng, M. Li and C. Li, *Phys. Chem. Chem. Phys.*, 2011, 13, 4715-4723.

61. H. Zhang, X. Lv, Y. Li, Y. Wang and J. Li, *ACS Nano*, 2009, 4, 380-386.

62. Q. Xiang, J. Yu and P. K. Wong, *J. Colloid Interf. Sci.*, 2011, 357, 163-167.